Structural Engineering and Mechanics, Vol. 13, No. 2 (2002) 171-186
DOI: http://dx.doi.org/10.12989/sem.2002.13.2.171

Penetration mechanisms of non-deforming projectiles into reinforced concrete barriers

Avraham N. Dancygier† and David Z. Yankelevsky‡

Department of Civil Engineering and National Building Research Institute, Technion, Technion City, Haifa 32000, Israel

Abstract. Static and dynamic penetration tests of reinforced concrete (RC) slab specimens are described and discussed. The experimental study was aimed at a better understanding of mechanisms that are involved in dynamic penetration, through their identification in static tests, and by establishing their relative influence in similar dynamic cases. The RC specimens were 80×80-cm square plates, and they were made of 30 MPa concrete. The non-deforming steel penetrator was a 50-mm diameter steel rod with a conical nose of 1.5 aspect ratio. Impact penetration tests were carried out with an air gun, which launched the projectiles at velocities of up to 300 m/sec. The static tests were conducted using a closed loop displacement control actuator, where the penetrator was pushed at a constant rate of displacement into the specimen. The static tests reveal important mechanisms that govern the penetration process and therefore contribute to a better understanding of RC barriers resistance to non-deforming projectiles impact.

Key words: impact; penetration; perforation; reinforced concrete barriers.

1. Introduction

The problem of reinforced concrete (RC) plates that are punched by a rigid, non-deforming body is of great concern in a wide range of applications, under static and dynamic conditions. A most common static application is the design of RC flat slabs without beams supported by columns, and typical dynamic applications are protective structures and structural elements in nuclear power plants.

Studies of static punching resistance in RC slabs show that punching resistance depends on the concrete's tensile strength, slab thickness, and reinforcement ratio (e.g., Menétrey 1996). Yankelevsky *et al*. (1980a and b) and Forrestal *et al*. (1988) analyzed dynamic penetration of ogive-nose penetrators. They showed that the forces on all ogive-nose shapes at small penetrator's velocities are similar and approach a quasi-static value. Forrestal's analysis indicates that as the velocity increases, blunter noses have larger forces.

The dynamic penetration and static punching theories conform to empirical observations. When a penetrator dynamically impacts a RC slab, the following types of damage and mechanisms are observed: front and rear crater formation, radial cracking, rear face radial and tangential cracking, penetration through concrete, shear failure and concrete plug formation (e.g., Yankelevsky 1997).

† Senior Lecturer
‡ Professor and Head

Based on the developed damage modes it may be assumed that static and dynamic penetrations of a similar penetrator involve similar mechanisms, with the exception of a front crater development and the effects of strain-rate (e.g., Hughes 1984), inertia and wave propagation, which refer to the dynamic case only. Despite the similarity of the damage modes, the approach of evaluating the dynamic punching resistance in RC is entirely different than the approach of evaluating the static resistance, and the parameters involved are different as well. The apparent similar damage observations on the one hand and the different modeling and theoretical solutions on the other hand, require further examination of the relationship between static and dynamic penetration of non-deforming penetrators into RC barriers.

Therefore, further studies of both static and impact resistance of RC barriers may contribute to the understanding of the penetration of non-deforming penetrators. Such study should identify the mechanisms that are common to both processes, and their contribution to the overall dynamic resistance. This paper describes results of an experimental program, aiming at the achievement of the above goals, and shedding more light on the mechanical development of the resistance and damage under both static and dynamic events. In this study static and dynamic penetration tests of RC slab specimens were carried out. The RC slab specimens in the static and in the dynamic tests were similar, and they were dynamically impacted and statically penetrated by similar non-deforming steel penetrators. Discussion of the static results and of their comparison with the dynamic response is presented.

2. Experiments

2.1. General

The experimental program consisted in testing similar specimens with similar penetrators in both static and dynamic tests. Thus, the results of the two types of tests can be compared. The penetrator was a 1.5-Kg, 50-mm diameter rod, made of hardened steel, with a sharp conical nose of 1.5 aspect ratio. The RC specimens were square, $80 \times 80 \times 20$ cm plates. They were made of ready-mixed concrete that consisted of ordinary Portland cement with a nominal fly ash content of 10% and had a 127-mm (5”) slump, and a 19-mm maximum aggregate size. The reinforcement was made of standard deformed steel bar meshes (400 MPa nominal yield strength and a minimum ultimate strain of 12%): $\phi 8$ mm@200 mm (each way) near the front (impacted or penetrated) face, and $\phi 8$ mm@100 mm (each way) near the rear face. The meshes’ arrangement ensured that none of the reinforcement rebars crossed the plate’s center, and hence, that the penetrator would not hit (or push) any of the steel rebars. The concrete cover of the reinforcement meshes was 15 mm on each side. The concrete’s average cube strength at 28 days ranged between 30 and 40 MPa.

2.2 Impact penetration tests

2.2.1 Setup

Impact penetration tests were carried out with an air gun, which launched the projectiles at striking velocities of up to about 300 m/sec. The plate specimens were mounted on a stationary stiff steel frame in front of the gun. They were supported (by the steel frame) along their perimeter to prevent movement in both directions, but no special measures were taken to provide a fully fixed

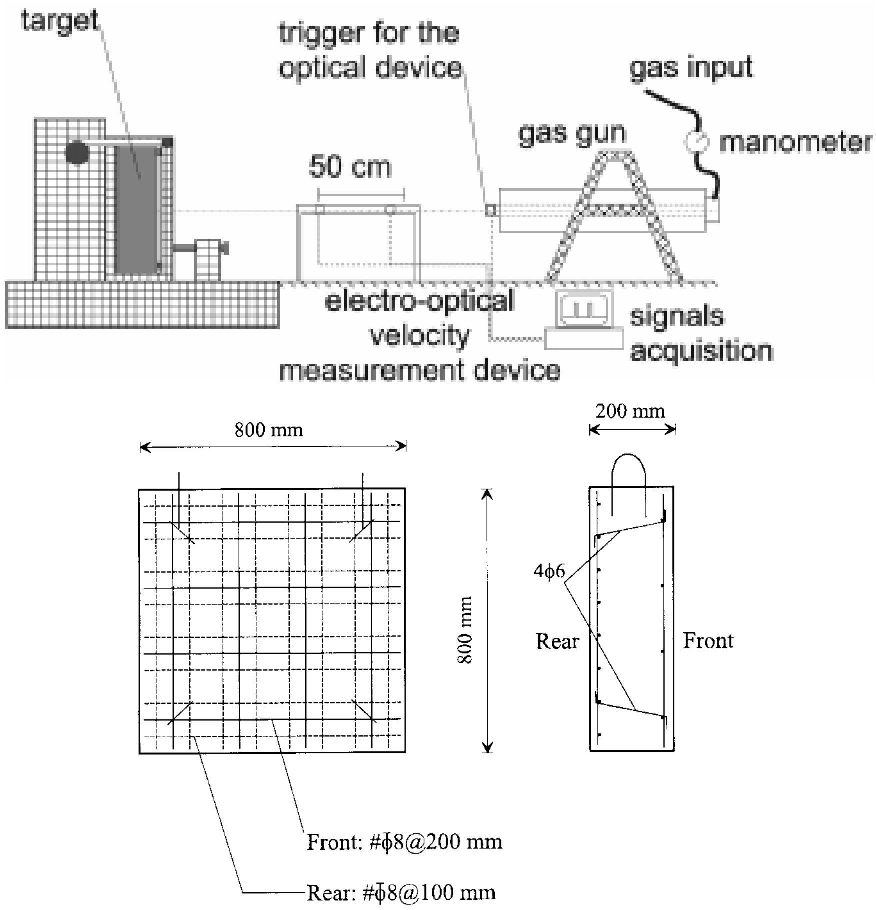

Fig. 1 Setup of the impact tests and slab specimens

boundary condition. Therefore the boundary conditions of the plates may be considered as a simple support (70 × 70-cm clear span). A schematic description of the impact experimental setup is shown in Fig. 1.

2.2.2 Results

The damage level of the plate specimens at different projectile's striking velocities was described and recorded according to a six-level qualitative scale, which was defined based on the plate's rear damage level and on its overall resistance, as follows:

(1) No visible damage to hairline cracks at the rear face;
(2) Visible cracks without scabbing;
(3) Heavy cracking, pattern of rear crater is shown indicating either *scabbing limit* or the development of a rear plug. The projectile's velocity at this damage level was denoted V_{sc};
(4) Rear face scabbing and spalling without perforation;
(5) Perforation of the specimen without projectile's full penetration through the target. When the projectile was stuck in the target a Perforation Limit (PL) was marked. The projectile's perforation limit velocity is denoted V_{pl};

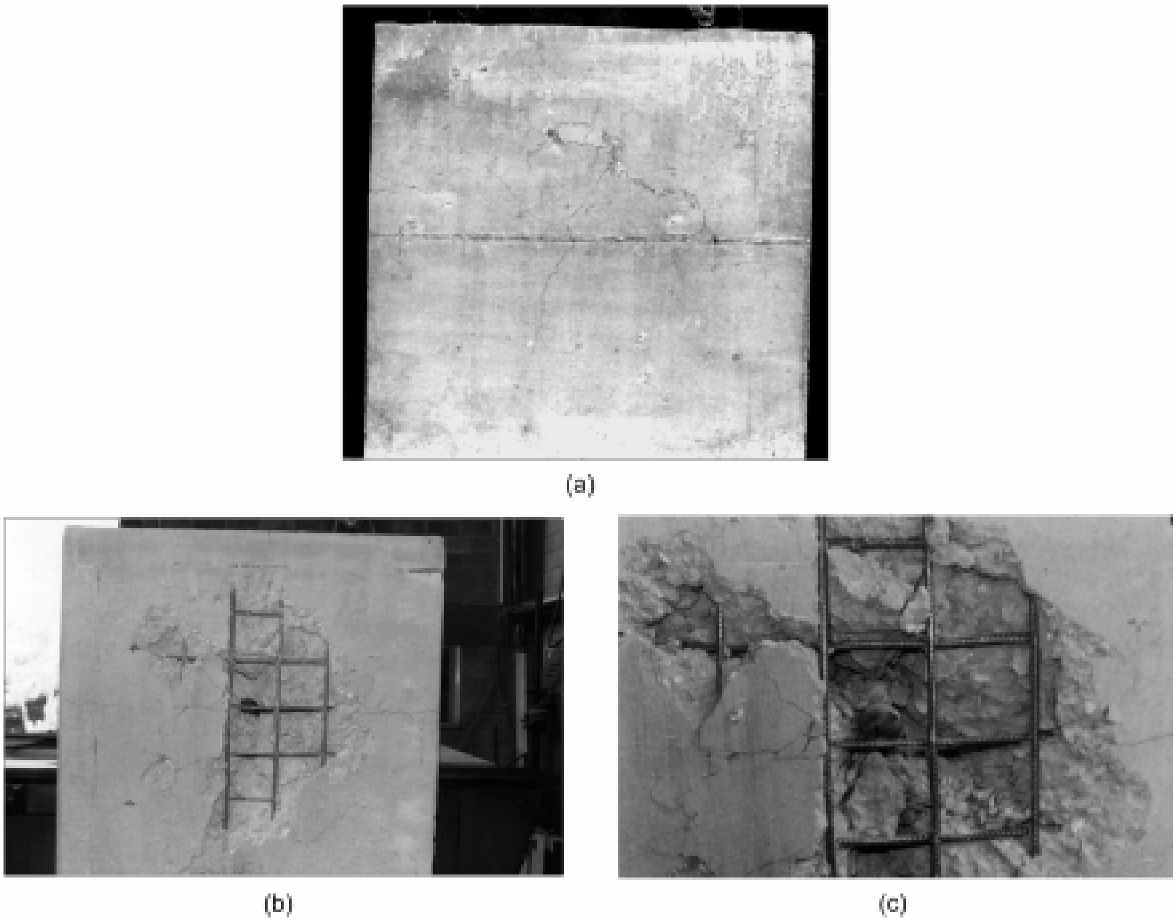

Fig. 2 Limits of impact resistance: (a) “Scabbing” limit, (b) and (c) perforation limit

(6) Projectile perforated the plate and exited with a residual velocity.

Fig. 2 shows typical rear face damage at the scabbing and perforation limits. The perforation limit velocity, V_{pl}, that was obtained from 13 specimens was 245-250 m/s. Rear face cracking pattern that indicates the initiation of a crater was obtained at a striking velocity, V_{sc}, of 200-205 m/s. Average front and rear face craters' diameters, D, were evaluated from $D = \sqrt{d_1 d_2}$, where d_1 and d_2 are measured crater's longest diameter and its perpendicular diameter, respectively. Table 1 summarizes the observed and measured results of the impact tests. The equivalent front and rear craters' diameters are also shown in Fig. 3. It can be seen that in the dynamic tests the average front and rear crater diameters ranged between 250 mm and 375 mm, and between 400 mm and 550 mm, respectively (Table 1 and Fig. 3).

2.3 Static tests and their results

2.3.1 Setup and test plan

The static tests were conducted with a closed loop displacement control actuator, where the penetrator was pushed at a constant rate of displacement into the specimen. Measurements were

Table 1 Impact tests results

Specimen	Vs (m/s)	Damage level	V_{sc} (m/s) measured	V_{sc} (m/s) NDRC (Barr)	V_{pl} (m/s) measured	V_{pl} (m/s) NDRC (Barr)	Front crater d_1 (mm)	Front crater d_2 (mm)	Front crater D (mm)	Rear crater d_1 (mm)	Rear crater d_2 (mm)	Rear crater D (mm)
20-1	296	6					340	300	319	530	475	502
20-2	289	6					340	300	319	475	350	408
20-3	248	5					325	310	317	660	330	467
20-4	250	6					340	310	325	510	340	416
20-5	216	4					380	370	375	410	410	410
20-6	199	2	200-205	156	245-250	255	350	295	321	–	–	–
20-7	211	2		(147)		(236)	360	305	331	–	–	–
20-8	204	2					Not measured			Not measured		
20-9	199	2-3					340	280	309	–	–	–
20-10	204	3+					350	280	313	540	430	482
20-11	203	3-4					300	260	279	500	380	436
20-12	250	6					270	230	249	540	510	525
20-13	245	5					350	340	345	560	530	545

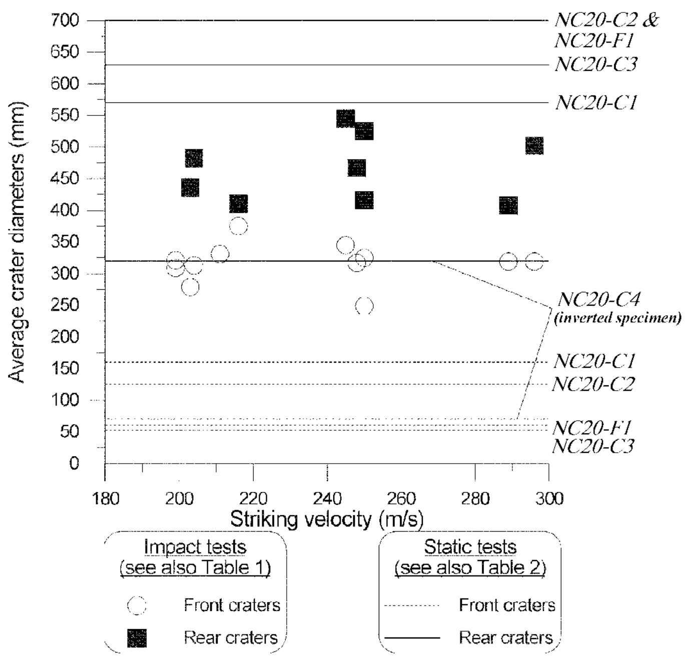

Fig. 3 Front and rear average crater diameters of static and dynamic tests (at various striking velocities)

taken of the load, of the penetrator and slab's rear mid-point displacements, and of the radial strains at the penetrated face of the plate specimens. The strain-gages were attached at 210 mm from the plate's center. The plates were simply supported by a steel frame with a clear span of 70 × 70 cm. Thus, both the boundary conditions and the supports-scheme were identical in the static and in the dynamic tests. Six tests were performed, four with a penetrator's conical nose shape (NC20-C1-4 in

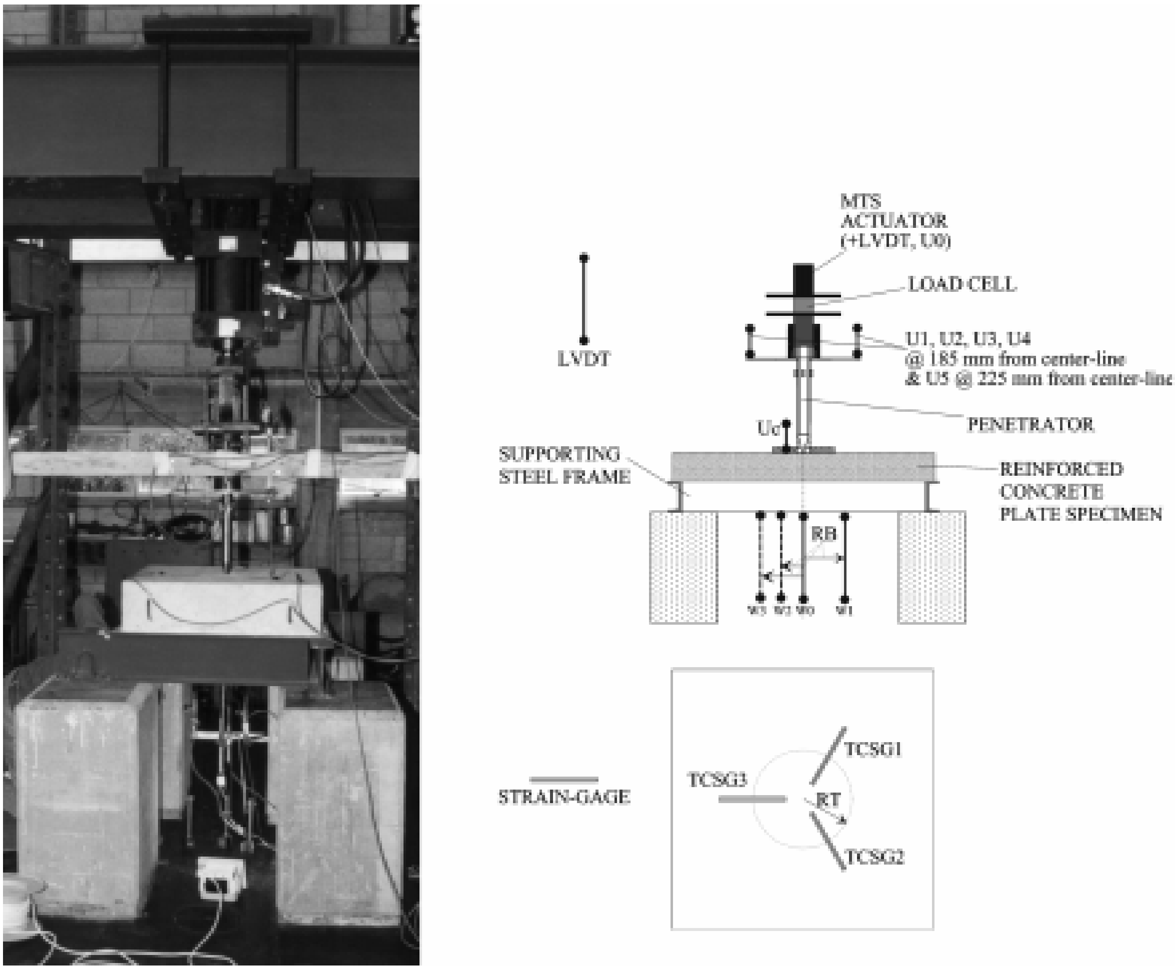

Fig. 4 Setup of the static tests

Table 2), and two with a flat nose. All specimens but one had a 200-mm thickness. The last test with the flat nose was performed on a thicker 250-mm slab (test NC25-F1 in Table 2). The first two tests were conducted with similar specimens. Test NC20-C3 included an annular steel disk with an inner 52-mm diameter and a 300-mm external diameter. The disk was 20-mm thick and it was glued to the specimen's top surface at its center. The purpose of the ring was to examine its effect on restraining the top radial strains. The effect of the front and rear reinforcement on the penetration process and on the resistance was examined in test NC20-C4, where the specimen was inverted, and the denser reinforcement was located near the top surface. Other data are given in Table 2 and the experimental setup is schematically shown in Fig. 4.

It is noted that in addition to the front face penetration and the rear crater formation, which were described in the introduction, the current static tests involved also bending of the slab, associated with top and bottom face displacements. According to these mechanisms, the problem's different displacement variables are schematically shown in Fig. 5, and they include the total penetrator's stroke, U_0, the top and bottom surface displacements, U_c and W_0 (respectively), the total penetration,

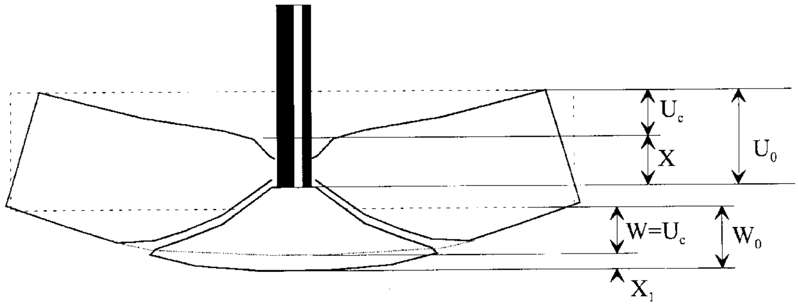

Fig. 5 Problem's displacement variables

X, and the rear shear-plug ejection, X_1. These variables have the following relationships and meanings:

$$X = U_0 - U_c \tag{1}$$
$$X_1 = W_0 - U_c \tag{2}$$
$$U_0 - W_0 = X - X_1 \tag{3}$$

Note that the difference $X - X_1$ in Eq. (3) is equal to the net projectile's penetration into the concrete Fig. 5, and that a rigid body ejection of the rear plug (pushed out by the projectile) is indicated when $\dot{U}_0 = \dot{X}_1$, i.e., when:

$$U_0 - X_1 = U_0 - (W_0 - U_c) \approx U_0 - \mathrm{W}_0 = X - X_1 = \text{Const.} \tag{4}$$

Table 2 Static tests data

Specimen	Cube strength(1) (MPa)	Specimen's thickness (mm)	Nose type	Peak load (kN)	Equivalent craters' diameters, D (mm)		V_p (stat.(3)) (m/s)	V_p (dyn.(4)) (m/s)	Notes
					Front	Rear			
NC20-C1	45	200	conical	270.58	160	570	153	241	Rear crater was broken into several pieces
NC20-C2	45	200	conical	292.82	125	700	129	230	Rear crater was broken into several pieces
NC20-C3	35	200	conical	267.28	52 (2)	630	134	183	
NC20-C4	35	200	conical	192.99	70	320	132	169	Inverted Specimen (denser reinforcement near the top surface)
NC20-F1	35	200	flat	300.47	60	700	84	145	Rear crater was ejected in one piece
NC25-F1		250	flat	437.22	57	750	98	175	Rear crater was ejected in one piece

(1) At 28 days;
(2) A 20-mm annular steel disk with an inner 52-mm diameter and a 300-mm external diameter was glued to the specimen's top surface at its center;
(3) Stress-rate effect was not included.
(4) A constant stress-rate factor of 5.0 was included in the calculations.

2.3.2 Results

Table 2 summarizes the observed and measured results of the static tests. In the 200-mm thick specimens with the conic nose penetrator and the denser reinforcement mesh near the rear (bottom) face, the peak penetration load ranged from 267 kN to 271 kN. When the top reinforcement was denser than the bottom one the peak load was only 193 kN (inverted specimen, NC20-4 in Table 2). The flat nose penetrators yielded higher peak loads of 300 kN and 437 kN in the 200-mm and 250-mm thick plates (respectively). These penetrators also caused craters' diameters that were larger at the bottom face and smaller at the top face, compared to those that were caused by the conic nose penetrators (see Table 2 and Fig. 3). Figs. 6, 7 and 8 show results of the static tests: Fig. 6 shows all the load-stroke (F vs. U_0) curves and two typical curves, which were obtained from tests NC20-C1 and NC20-F1 that were performed with conic and flat nose penetrators (respectively). Fig. 7 shows the relations between the net penetration ($X - X_1$) and the total penetrator's stroke (U_0), which were obtained from two tests with conic nose penetrators (NC20-C1 and the inverted NC20-C4) and from the flat nose penetrator test (NC20-F1). Fig. 8 shows these tests' results, which include the load, displacements, and top radial strains as a function of the total stroke, U_0.

At a total stroke of 100 to 150 mm the resistance of the plates was decreased to a magnitude of about 10% of the peak load and the specimens were perforated.

No unique response was observed of the NC20-C3 specimen, which had an external rigid annular steel disk glued to its front face (Table 2 and Fig. 6a), except for the smaller front crater bounded by the steel ring.

The static tests' results indicate three phases that characterize the penetration process of the conical penetrator. In the first phase, which was also identified by others (e.g., Dinic and Perry 1990, Yankelevsky 1998), there is a front (or top) penetration, which creates large volume changes in the concrete as the penetrator's nose is pushing forward. During this phase the penetration is resisted mainly by the compressive strength of the concrete front face layer. It should be noted that this strength is a function of the spatial stress distribution around and in front of the penetrator's tip. The resistance force peaks within a realtively small stroke of 20 to 30 mm at the penetrator's conic nose tip, and a stroke of 10 mm at the tip of the flat nose (Fig. 8a, b and Fig. 8c, respectively). This

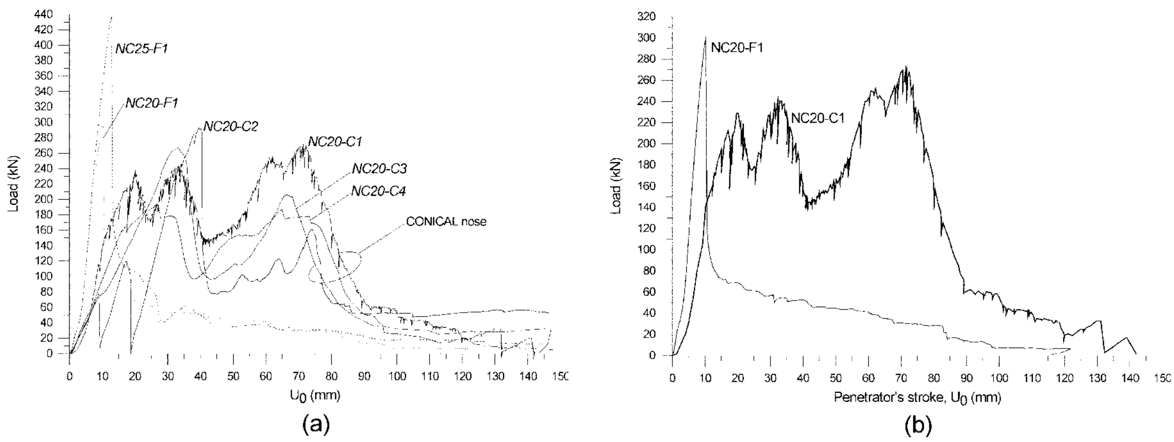

Fig. 6 Curves of static load-total penetrator's stroke of (a) all static tests, and of (b) two typical tests with a conical penetrator's nose (NC20-C1) and a flat nose (NC20-F1)

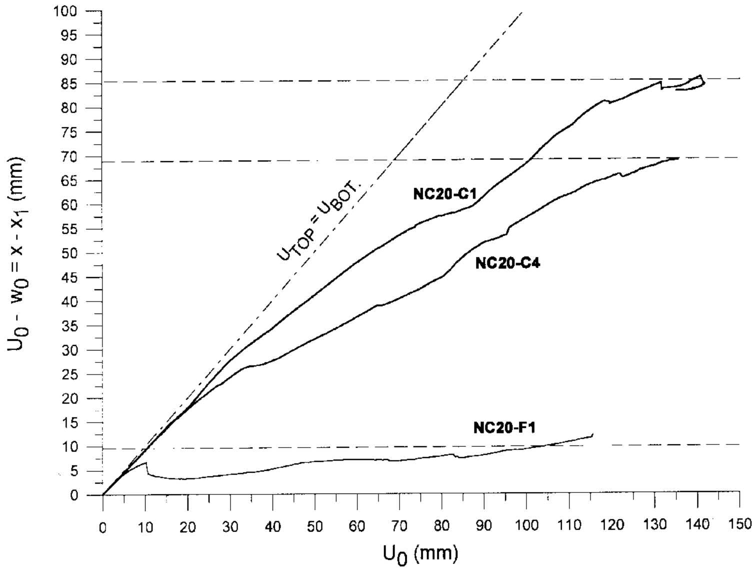

Fig. 7 Relative displacement curves in the static penetration tests (NC20-C4: overturned specimen; NC20-F1: flat nose)

phase is also typified by relatively small bottom bending displacement, W_0 ($U_{TOP} = U_{BOT.}$ in Fig. 7, and small W_0 values in Fig. 8). Increasing radial strain at the penetrated face of the plate (dashed lines in Fig. 8) indicates both phenomena. The plate's bending during the initial phase is indicated by the bottom radial cracks that were the first to develop (Fig. 9a).

When a shear plug develops the barrier's resistance decreases, followed by a second peak of the load for the sharp conical nose. It is interesting to note that the second peak occurred when the penetrator's tip reached a depth of about 75-mm, which was equal to its nose length. The second peak was not observed in the flat nose tests (NC20-F1, Figs. 6, 7 and 8).

In a third and final phase the developed shear plug is pushed out from the plate's rear face by the penetrator. The rigid body displacement is indicated in Fig. 8 by a constant relative displacement, i.e., by $\dot{U}_0 = \dot{W}_0$ or $U_0 - W_0 = \text{const}$. A residual resistance during this phase is shown in Fig. 6 by the load values at $U_0 > 10$ mm in NC20-F1 and at $U_0 > 90$ mm in NC20-C1. It may be attributed mainly to the dowel action of the reinforcement rebars, which at this stage were already bent down by the ejecting plug, and contributed a vertical force component to resist its downward displacement. In fact, in tests NC20-C1 and NC20-F1 some rebars failed in tension.

Compared to the dynamic tests, the static tests resulted in average craters' dimensions (D) that were smaller in the specimens' front face and larger in their rear face (Table 2 and Fig. 3).

3. Discussion

3.1 Dynamic tests results

The perforation limit velocity, V_{pl} that was obtained in the experiments (250 m/s) agrees well with the predictions of known penetration formulae. For example, it is different by only 2% to 6% from

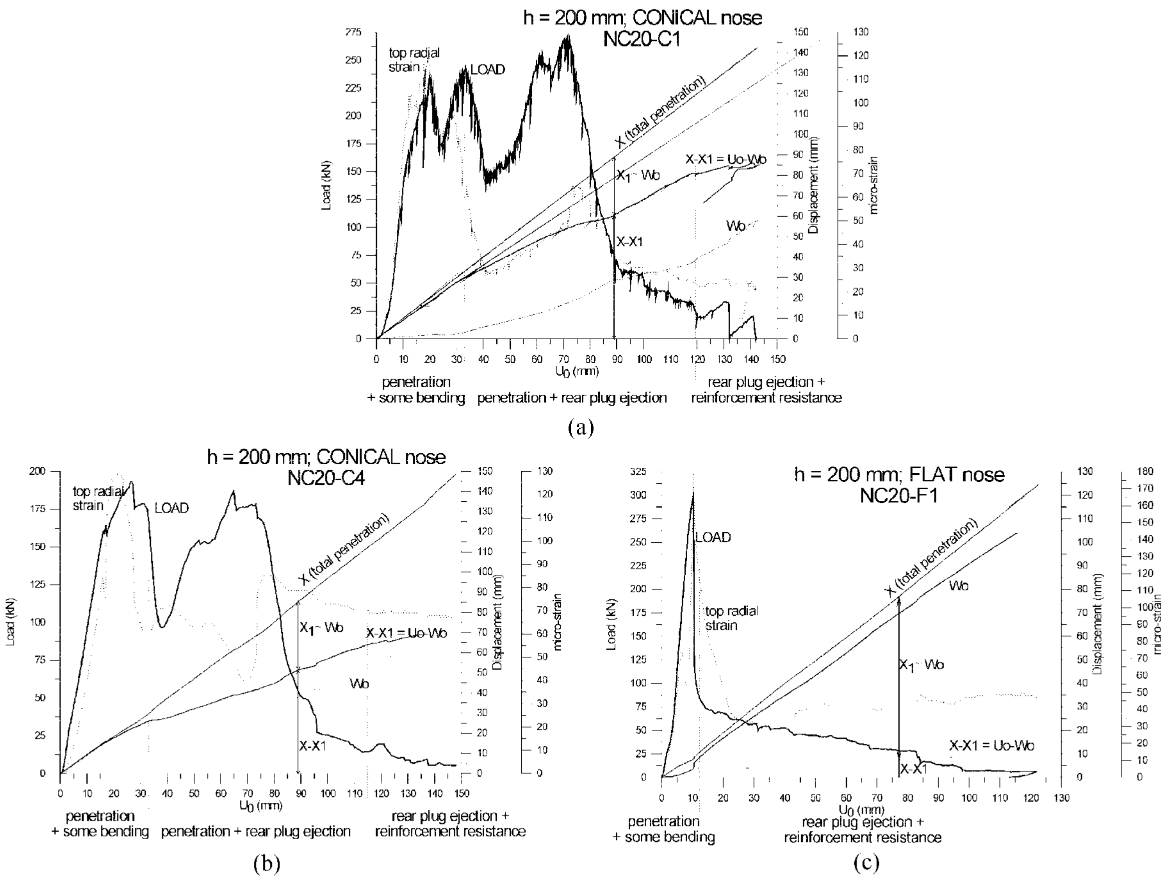

Fig. 8 Loads, top radial strains and mid-bottom displacements in (a) NC20-C1, (b) NC20-C4 (overturned specimen) and (c) NC20-F1 (flat nose)

the prediction of the NDRC equations (Kennedy 1976) or that of Barr equations (Barr 1990), according to which, for the tested specimens and projectile's properties, $V_{pl} = 255$ and 236 m/s, respectively (Table 1).

However, these formulae predict a much lower velocity at the "scabbing" limit (156 and 147 m/s, respectively). This difference between the theoretical and experimental scabbing limit velocities indicates a rear face damage mechanism in the current tests that was different than the classical scabbing, related to the reflected tension wave. In fact this result shows that a development of a rear shear plug, which was observed in the second phase of the static tests, occurred also in the dynamic punching tests. Thus, the "classical" wave propagation-induced scabbing velocity (150 m/s) of the current projectile's mass (1.5-Kg) did not cause at the barrier's thickness that was tested (200-mm) visible rear face damage. However, a shear-plug formation at higher striking velocities of about 200 m/s induced initiation of rear face cratering that was identified as the first damage limit (comparable to the "scabbing limit"). Dinic and Perry (1990) reported a similar rear face damage mechanism.

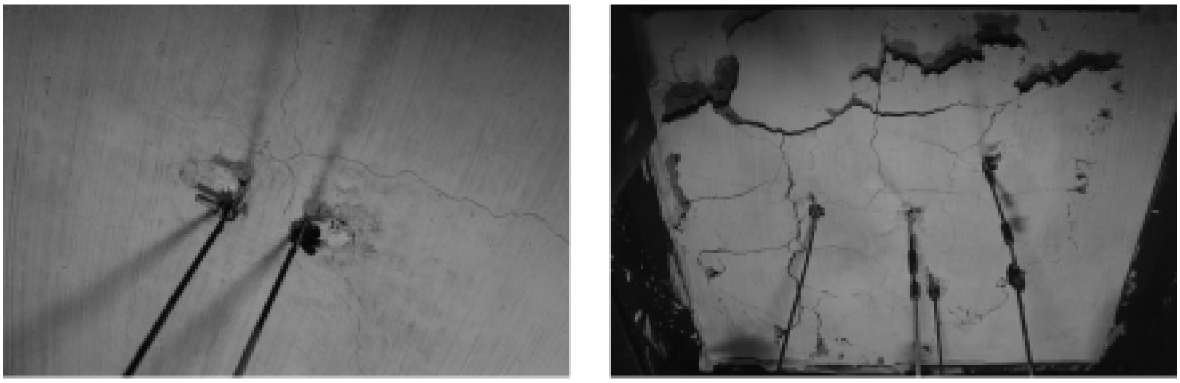

(a) radial cracking during the initial phase (b) crater formation during second and third phases

Fig. 9 Rear face damage during static penetration

3.2 Static tests results

3.2.1 Target resistance

The peak static loads developed on a conical nose during the penetration's first phase indicate contact pressure of the order of several hundreds MPa (Fig. 10a), which is more than an order of magnitude larger than the concrete uniaxial compressive strength. That level of compression stress may be developed due to increasing confinement conditions around the penetrator's nose with increasing penetration depth. The bending of the plate, which creates a triaxial state of stress, further increases the confinement conditions.

3.2.2 Nose shape effect

Higher peak loads were measured under the flat nose penetrators (Table 2), although, considering the horizontal projection of the conical nose contact area, they yielded smaller average vertical contact stresses due to the relatively large contact area. However, as soon as a forged conical concrete nose is developed in front of the projectile (Hawkins 1968) the sliding surface geometry controls the contact stress magnitude. Rear and front craters' diameters that were caused by the flat and conical nose penetrators were also different, as described in the results-section (2.3.2).

From the measured results it is noted that while the initial phase occurred within about 30-mm penetration depth of the conical penetrator into the specimen, in the tests with the flat nose penetrator this phase occurred only within the first 10-mm of the penetration depth (Fig. 8). Additionally, the second peak that was observed under the conical nose penetrator was not observed in the flat nose tests (NC20-F1, Figs. 6 and 8). Thus, when a flat-faced penetrator was tested the initial and final penetration phases described above (section 2.3.2) governed the response without the development of the second phase.

The static results of a flat nose penetrator may resemble and thus be compared to the punching capacity of reinforced concrete slabs. For example, the predicted capacities of the 200-mm and the 250-mm thick slabs according to Menétrey (1996) are 266 kN and 284 kN, respectively. These analytical values that were calculated with the data obtained before and during the tests, Table 2 (i.e., including the rear crater diameters for the calculation of the concrete cone's inclination) are 89% and 65% of the measured capacities. While the former prediction approximately agrees with

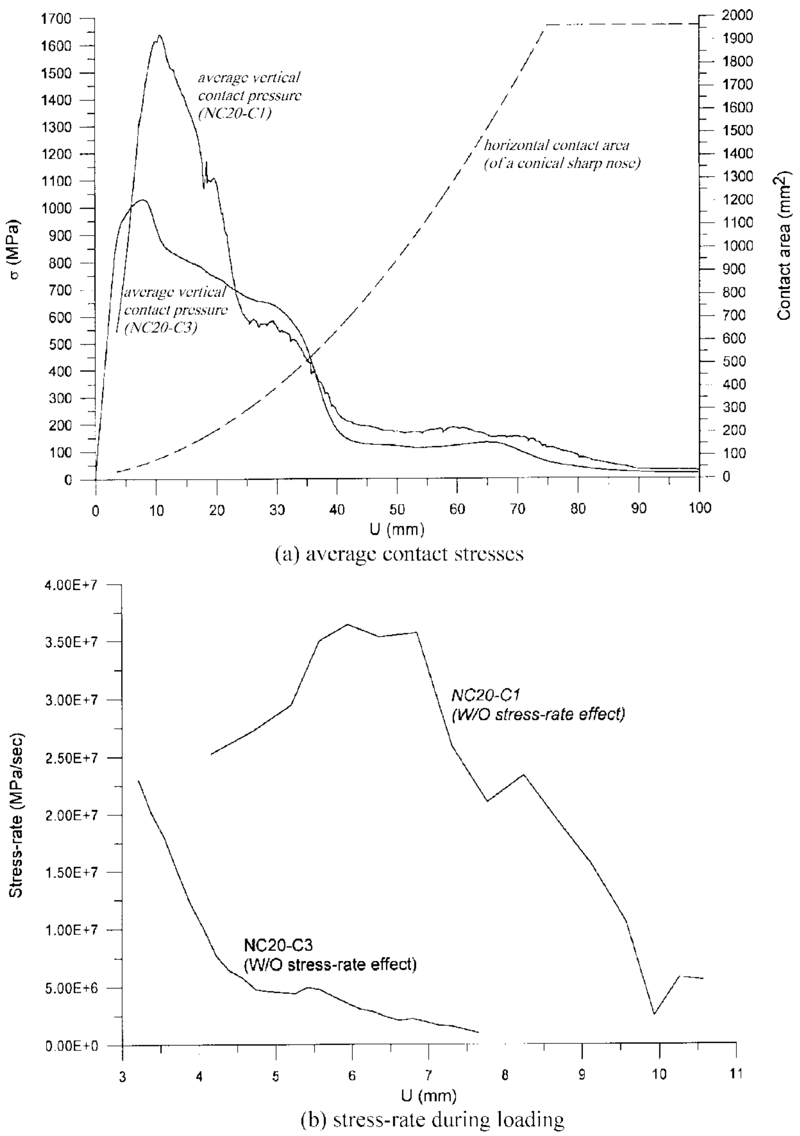

Fig. 10 Contact pressures in tests NC20-C1 and NC20-C3

the experimental result, the latter is much lower. It is noted, however, that for the 250-mm thick slab a 965-mm rear crater would have yielded a theoretical capacity equal to the experimental one. It is therefore concluded that this difference was due to the physical dimensions of the 250-mm slab, which developed a rear crater diameter that was equal to the slab's span (750 mm, Table 2). It should also be noted that the above theoretical capacities include a contribution of the dowel action by the reinforcement mesh, which is 20% of the total resistance (an average value deduced from experimental results given by Menétrey, 1996).

3.2.3 Reinforcement effect

The overturned specimen of test NC20-C4 showed lower resistance (Fig. 8 and Table 2). This result demonstrates the effect of the front and rear reinforcement ratios and densities on the plate's penetration resistance, noting that these were the only significant differences between this and the other preceding tests. Furthermore, the relatively small front crater's diameter of specimen NC20-C4 (Table 2) indicates an increased confining effect of the denser front reinforcement of this specimen. A similar result was obtained in test NC20-C3, which had a thick circular ring glued to its front face, although its rear reinforcement ratio was not reduced. The smaller front craters in tests NC20-C3 and NC20-C4 were not accompanied though, by an initial increase of the plate's resistance as could have been expected from the increased front radial confinement.

3.3 Comparison between dynamic and static tests results

3.3.1 Observed damage

The dynamically induced rear craters were smaller than those of the static tests, while the impacted specimens had larger front craters compared to those of the static tests (Fig. 3). It is interesting to note that in test NC20-C4 the rear crater's average diameter was significantly smaller compared to those of the other tests. This specimen was overturned, thus its rear reinforcement ratio was half of those in the other tests, with larger spacing between the rebars. It exhibited lower peak resistance (Table 2) but smaller rear damaged area.

The smaller statically induced front craters may be attributed to the overall influence of the dynamic inertial effects (see 3.3.3).

3.3.2 Resistance

Pseudo-dynamic velocity time-histories can be obtained from the empirical static load (F)-displacement (U) curves (e.g., Fig. 6) by their numerical integration, as follows:

$$\int_{V(U=0)}^{V(U)} MVdV = -\int_{0}^{U} F(\bar{U})d\bar{U} \tag{5}$$

or,

$$V^2 = V_0^2 - \frac{2}{M}\int_{0}^{U} F(\bar{U})d\bar{U} \tag{5a}$$

where M is the projectile's mass (1.5 Kg) and V is its instantaneous velocity, which in Eqs. (5) and (5a) is a function of the instantaneous penetration, U. V_0 is the projectile's striking velocity, $V(U = 0)$. Time history is obtained from the above integration according to the kinetic relation, $V(U)\cdot\Delta t = \Delta U$, where Δt is the time interval between two measured points of U. A perforation limit velocity, V_p, is an initial striking velocity V_0 that would result in a zero residual velocity at $U = h$ ($V(U = h) = 0$), where h is the barrier's thickness (200 mm). Thus, according to Eq. (5a), V_p is given by:

$$V_p = \sqrt{\frac{2}{M}\int_{0}^{h} F(U)dU} \tag{6}$$

Values of V_p according to the measured static resistance are given in Table 2.

Processing the static force-displacement curves of the tests with the conical nose yielded impact velocity values of 129 to 153 m/s (V_p (stat.) in Table 2), which are about 40% lower than the experimental results of the impact tests. This result indicates the importance of the static component in the overall resistance to hard projectile penetration. However, it also shows that the concrete strain-rate sensitivity, which was not taken into account in these calculations, becomes an important factor in increasing the concrete resistance under dynamic punching.

Fig. 10a shows the average vertical stress under the conical penetrator's nose in tests NC20-C1 and NC20-C3. The stress-rates during the loading phase in these tests are shown in Fig. 10b, following the procedure described above (Eq. 5 or 5a). It can be seen that even according to the static measurements a loading stress-rate in the order of 10^7 MPa/sec is expected to be developed during a dynamic punching. Considering the concrete strength, and following Ammann and Nussbaumer (1991) (Fig. 11), a stress-rate factor of 4 to 5 may be applied in order to evaluate the dynamic resistance. Velocity versus time curves of tests NC20-C1 and NC20-C3 are shown in Fig. 12 together with the predicted curve according to the NDRC equation for the dynamic penetration into an infinitely thick barrier (Kennedy 1976). It can be seen that up to about 0.5 msec the curve that was calculated from the current static tests, taking into account a constant stress-rate factor of 5 (only during loading) resembles the NDRC curve. The divergence of the velocity-time curve from the prediction of the NDRC equation, at $t > 0.5$ msec, indicates rear face effects and the influence of a rear crater that are expected to develop after the initial penetration phase.

3.3.3 Inertial effects

The second and third penetration phases, which were depicted from the static tests, may show different barrier's resistance under impact conditions due to the concrete plug's inertia. Furthermore, it is expected that under dynamic punching the plate's inertia would eliminate the statically observed initial phase of bending, and induce a more local response.

Other inertial effects include the compression and tension wave propagation through the concrete slab's thickness, and the dynamic bending re-bound. It is noted that the dynamic re-bound of the

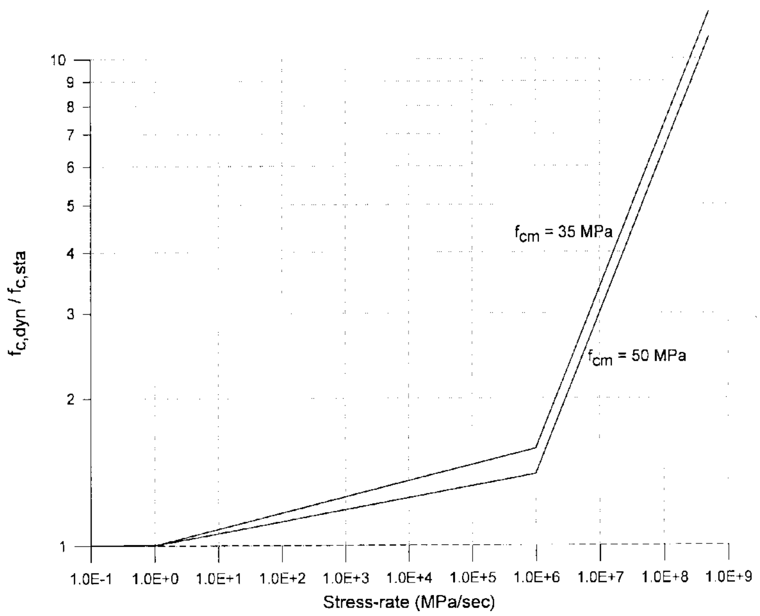

Fig. 11 Concrete stress-rate factor in compression (Ammann and Nussbaumer 1991)

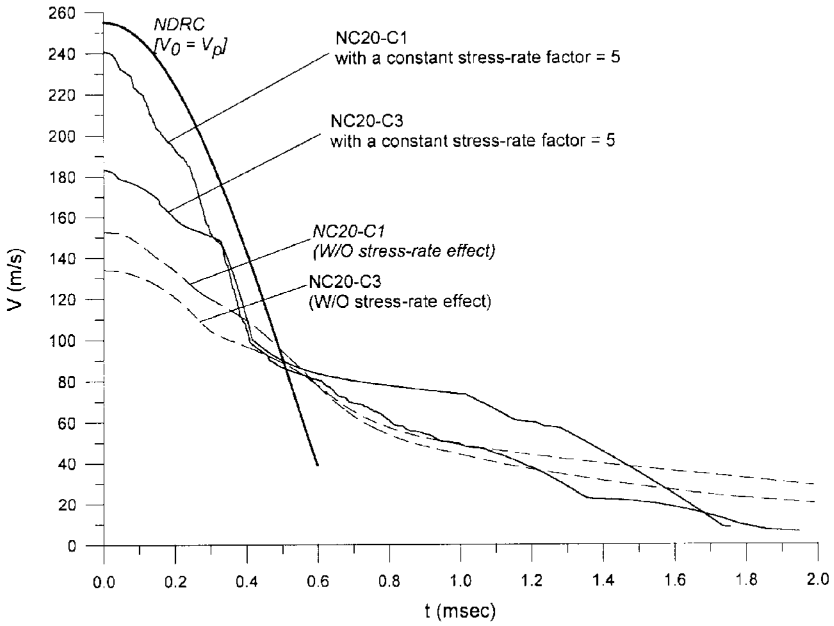

Fig. 12 Velocity time-histories during dynamic punching of tests NC20-C1 and NC20-C3

plate, which does not occur in the static tests, takes place only in the later part of the response after most or all of the dynamic punching process is completed. However, the observed dynamic damage, like that of the front face crater, is a result of the overall specimen's response until it comes to rest. This includes inertial effects such as the plate's re-bound.

4. Conclusions

Static and dynamic penetration tests of reinforced concrete barriers were carried out. The experimental study was aimed at a better understanding of mechanisms that are involved in dynamic penetration, through their identification in static tests, and by establishing their relative influence in similar dynamic cases.

The results of the dynamic tests showed good agreement (2% to 6% difference) with theoretical predictions of known penetration formulae for the perforation limit velocity. For the scabbing limit velocity however, much poorer agreement was obtained, indicating that in addition to the known wave propagation effect, a mechanism involving a shear plug formation in the concrete may also affect the RC barrier's lower damage-level limit.

The static test results show different phases of the penetration process. An initial penetration phase was identified, which is characterized by volume changes in the concrete. This phase was followed by shear plug formation, which is finally pushed out by the penetrator, resisted at that stage only by the bent rear mesh reinforcement rebars. When a flat-faced penetrator was tested the above-described initial and final penetration phases governed the response without the development of the second phase.

The static penetration tests support the two-phase dynamic penetration model, which assumes a phase of penetration without rear face effects, followed by a phase of rear plug formation that affects the penetration resistance (Yankelevsky 1997).

Comparison between the static and the dynamic results was done by means of integrating the statically measured load-displacement curves. This comparison showed that the static resistance is of major importance, however, taking into account the concrete stress-rate sensitivity is essential for realistic analysis of a reinforced concrete barrier's response to an impact penetration of a hard projectile.

References

Ammann, W., and Nussbaumer, H. (1991), "Behavior of concrete and steel under dynamic actions", *CEB-Bulletin D'Information No 209 Vibrations Problems in Structures-Practical Guidelines*, 189-199.

Barr, P. (1990), "Guidelines for the design and assessment of concrete structures subjected to impact", *Report, UK Atomic Energy Authority, Safety and Reliability Directorate*, HMSO, London.

Dancygier, A.N., Yankelevsky, D.Z., and Baum, H. (1999), "Behavior of reinforced concrete walls with internal plaster coating under exterior hard projectile impact", *ACI Materials J.*, **96**(1).

Dinic, G., and Perry, S.H. (1990), "Shear plug formation in concrete slabs subjected to hard impact", *Eng. Fracture Mech.*, **35**(1/2/3), 343-350.

Forrestal, M.J., Luk, V.K., and Watts, H.A. (1988), "Penetration of reinforced concrete with ogive-nose penetrators", *Int. J. Solids and Struct.*, **24**(1), 77-87.

Hawkins, N.M. (1968), "The bearing strength of concrete loaded through rigid plates", *Magazine of Concrete Research*, **20**(61), 31-40.

Hughes, G. (1984), "Hard missile impact on reinforced concrete", *Nuclear Eng. and Design*, **77**, 23-35.

Kennedy, R.P. (1976), "A review of procedures for the analysis and design of concrete structures to resist missile impact effects", *Nuclear Eng. and Design*, **37**, 183-203.

Menétrey, P. (1996), "Analytical computation of the punching strength of reinforced concrete", *ACI Struct. J.*, **93**(5), September-October, 503-511.

Yankelevsky, D.Z. (1997), "Local response of concrete slabs to low velocity missile impact", *Int. J. Impact Eng.*, **19**(4), 331-343.

Yankelevsky, D.Z., and Adin, M.A. (1980a), "A simplified analytical method for soil penetration analysis", *Int. J. Analy. and Num. Meth. in Geomech.*, **4**(3), 233-254.

Yankelevsky, D.Z., and Gluck, J. (1980b), "Nose shape effect on high velocity soil penetration", *Int. J. for Mech. Sci.*, **22**(5), 279-313.